Numerical Study of Large Aspect-Ratio Synthetic Jets

B. R. Ravi* and R. Mittal†
Department of Mechanical & Aerospace Engineering,
The George Washington University,
Washington DC, 20052

Three-dimensional numerical simulations are performed to study the formation and evolution of large aspect-ratio synthetic jets. A rectangular synthetic jet of aspect-ratio (AR) 8.0 issuing into quiescent air at jet Reynolds number of 300 and Stokes numbers of 6.84 and a jet of infinite aspect ratio with jet Reynolds number 200 and Stokes number varying between 12 and 24, interacting with an external laminar boundary layer are examined in detail. For the quiescent jet, the results indicate the formation of vortex train which undergoes axis switching and consequently a complex topological evolution. Simulations for an infinite aspect-ratio jet interacting with a flat-plate boundary layer indicate that actuation frequencies much lower than the Tollmein-Schlichting frequencies are effective in triggering instabilities in the boundary layer which bring significant streamwise momentum in to the boundary layer thereby making the boundary layer more resistant to separation. Examination of the vorticity flux for jet in crossflow also indicates that this quantity varies linearly with the Strouhal number.

Nomenclature

A = Jet exit area for finite aspect ratio jet, $A = w \times d$
B_e = Jet width, $B_e = \left(v_{\min} + v_{\max}\right)/2$
D = Width of jet cavity
d = Jet width
f = Actuation frequency of synthetic jet
H = Shape Factor, $H = \delta^*/\theta$
H_c = Height of jet cavity
h = Jet height
Re = Reynolds number, $\mathrm{Re}_j = \bar{V}_j\sqrt{A}/\upsilon$, $\mathrm{Re}_d = \bar{V}_j d/\upsilon$, $\mathrm{Re}_\delta = U_\infty \delta/\upsilon$
S = Stokes number, $S = \sqrt{\omega A/\upsilon}$ (Finite aspect-ratio), $S = \sqrt{\omega d^2/\upsilon}$ (Infinite aspect-ratio)
St = Strouhal number, $St = \omega d/\bar{V}_j$
T = Forcing period, $T = 2\pi/\omega$
U_∞ = Freestream velocity
U_o = Velocity Amplitude
$\bar{V}_j$ = Average jet velocity
W = Spanwise width of jet cavity
w = Spanwise jet width
ν = Kinematic viscosity
δ = Boundary layer thickness
δ^* = Displacement thickness

* Graduate Research Assistant, Student Member AIAA.
† Associate Professor, Associate Fellow AIAA.

θ = Momentum thickness

Ω_v = Flux of vorticity

ϕ = Phase angle, degrees

ω = Angular frequency, rad/s

ξ = Vorticity, $\xi = \sqrt{\xi_x^2 + \xi_y^2 + \xi_z^2}$

I. Introduction

Synthetic jet devices are being used in a number of flow control applications ranging from thrust vectoring of jets[1] to boundary layers turbulence control[2-4], mixing enhancement[5,6] and active separation control[7-8]. These devices provide unsteady forcing which is more effective than pulsed or steady forcing. The actuation frequency can be tuned to suit the needs of a particular flow configuration and the device usually does not require complex fluid circuits. A typical jet actuator comprises of a cavity with an oscillating diaphragm and a slot or orifice from which the jet issues. A train of vortex rings is generated due to the time-periodic motion of the diaphragm imparting a finite momentum into the surrounding fluid with zero-net-mass-flux (ZNMF). Earlier works[9-11] related to interaction of these vortical structures with external flow field indicate the formation of closed recirculation zones leading to the modification of the base flow on scales that are larger than the characteristic length scales of synthetic jets.

Several experiemental techniques have been used in the past to examine ZNMF actuators. Earliest of the investigations due to Meissner[12], reports the study of attenuation of very high frequency acoustic waves within the body of a fluid. The attenuation of the transmitted sound waves due to viscous effects near solid boundaries was investigated by Andres and Ingard[13] at high Reynolds numbers. The effects of circulation caused by acoustic streaming were reported by Ingard and Labate[14] by studying the impedance of orifices by applying an orifice plate to a circular tube driven by sound waves. Acoustic streaming in the vicinity of the orifice was investigated for a round jet by Lebedeva[15] using high amplitude sound waves. By employing cavitation-controlled ultrasonic agitators Sheen et al[16] were able to generate streaming motions in water. Recently, Yao et al[17] have reported the velocity measurements of synthetic jets generated by time-periodic oscillation of wall-mounted piezoelectric diaphragm in an enclosed cavity and issuing into quiescent air. Three different techniques (PIV, LDV and Hot-wire anemometry) were used for the velocity measurements.

A limited amount of numerical work has been reported in literature on synthetic jets issuing into quiescent air. One of the earliest works was reported by Kral et al.,[18] by performing two-dimensional incompressible computations of both laminar and turbulent jets, the latter obtained as solution to the unsteady Reynolds-averaged Navier-Stokes (URANS) equations with one equation Spallart-Allmaras turbulence closure. The flow within the cavity was not modeled. They observed that the jet did not capture the break-up of vortex train whereas the turbulence model indicated that the counter-rotating vortices dissipate quickly. This was attributed to the lack of three-dimensionality in the model. Rizzetta et al[19] investigated synthetic jets flow fields numerically using DNS. They obtained solutions using the unsteady compressible Navier-Stokes equations for both the interior of the actuator cavity and the external jet flow-field. The velocity at the jet exit was recorded for one complete cycle once the internal cavity flow became periodic after several cycles and this was used as the boundary condition at the jet exit for subsequent computations without modeling the cavity flow thereafter. They then used higher order compact-difference schemes in association with non-dispersive spatial filters to solve for the external flow field. The use of three-dimensionality helped to capture the breakdown of the external flow into a turbulent jet.

Rampunggoon[20] performed two-dimensional numerical simulations to investigate the dynamics of the synthetic jets in the presence of cross-flow as well as jets issuing into quiescent air. A comprehensive parametric study was carried out where the diaphragm amplitude, external flow Reynolds number, boundary layer thickness, and slot dimensions were varied and the scaling of the jet characteristics with parameters examined. The so called "virtual aero-shaping" effect of synthetic jets was examined[11] and it was shown that the recirculation bubble length scales with the jet momentum coefficient. Utturkar et al.[21] have performed two-dimensional numerical simulations to study the sensitivity of synthetic jets to the design of the jet cavity. They considered the changes in the cavity aspect ratio as well as the placement of the oscillating diaphragms. Both quiescent and the external cross-flow have been investigated. The authors also proposed and validated a jet formation criterion $\mathrm{Re}_d / S^2 > K$, where K is around 2 and 0.16 for two-dimensional and axisymmetric synthetic jets, respectively[22].

In the study reported here, the fluid dynamics associated with large aspect-ratio synthetic jets are examined in detail as a sequel to the study of moderate aspect-ratio synthetic jets performed earlier[23] using three-dimensional

numerical simulations of incompressible Navier-Stokes equations on Cartesian grids. Since most synthetic jets used in practical applications are rectangular and finite aspect-ratio[5-8], it is important to understand the fluid dynamics of such jets. The geometrical configuration of the jet is similar to that of Kotapati et al[25] who used this configuration to validate simulations against the experiments of Yao et al[17]. The rest of the paper is organized as follows. The flow configuration used in the simulations is described in the next section followed by the description of the equations of motion governing the flow field and numerical methodology used. Results for the finite aspect-ratio jet are discussed in the following section. The last section focuses on the results obtained for infinite aspect ratio jets interacting with an external boundary layer

II. Flow Configuration

The geometry used in the computations is shown in the figure 1. The cavity is chosen to be rectangular and opens through a narrow rectangular orifice. The jet-exit center-line in the symmetry plane is chosen to be the origin of the coordinate system. The *x, y* and *z* directions represent the cross-stream, streamwise and the spanwise directions respectively. The cavity is characterized by a width (D), height (H_c), and a spanwise width (W). The jet is characterized by a width (d), height (h) and a spanwise width (w). For the finite aspect-ratio jet, the cavity spanwise width is chosen to be $20d$. The oscillatory motion of the diaphragm is modeled by specifying a uniform sinusoidal boundary condition at the cavity bottom as $U_o Sin(\omega t)$ where $\omega = 2\pi f$ and f is the synthetic jet actuation frequency. Details of the domain size, mesh size and the flow parameters are provided in the table 1 below and were

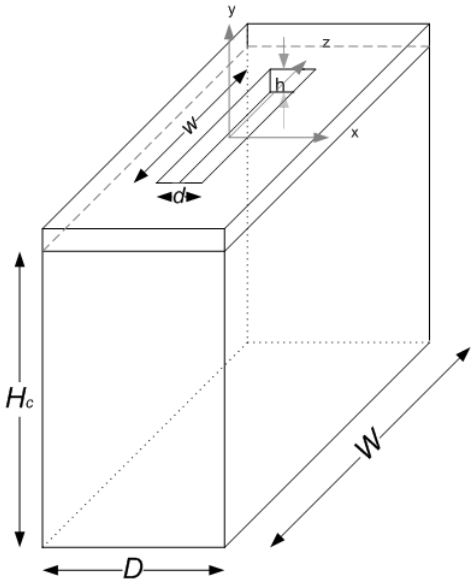

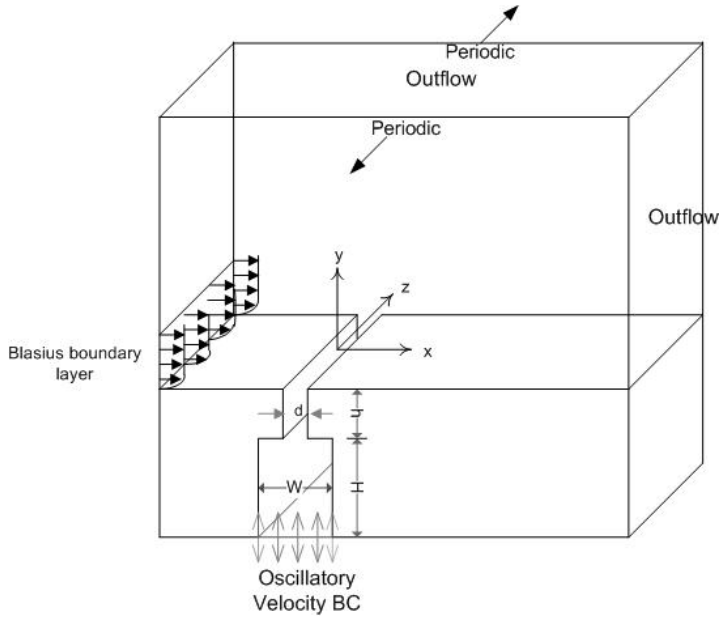

Figure 1a. Synthetic jet cavity and orifice for finite aspect-ratio jet

Figure 1b. Infinite aspect ratio synthetic jet with domain and BCs

chosen based on the earlier experience in generating meshes for moderate aspect ratio jets[23] so as to resolve the flowfield reasonably well. The various boundary conditions used in the computations are indicated in the figure 1. Two different flow cases are considered; first is that of finite aspect ratio (AR) jet in quiescent external flow and the second is an infinite aspect-ratio jet interacting with a laminar, flat plate boundary layer. For the AR=8 jet, outflow velocity boundary conditions are prescribed in all the directions above the jet exit plane whereas for the infinite aspect ratio jets the spanwise boundaries are forced to be periodic. A typical mesh used in the computations is shown in figure 2. A highly non-uniform mesh is used with clustering in the vicinity of the jet exit plane so as to capture the vortex structures and resolve the shear layer in the slot. The time step is chosen so as to provide 14000 time steps per cycle for the finite aspect ratio case and 2000-6000 time steps per cycle for the infinite aspect ratio jets. Typically about 5 – 6 cycles of the jet are simulated and flow statistics accumulated for the later cycles which ensure the elimination of any transient effects.

Table 1

Aspect Ratio	Flow Type	Domain Size	Mesh Size	Cycles Averaged
8	Quiescent	$320d \times 100d \times 320d$	105 x 236 x 105	3 – 6
Infinite	Crossflow	$40d \times 47.6d \times 4d$	201 x 138 x 33	3 – 6

III. Governing Equations and Numerical Methodology

The governing equations that are solved in order to obtain complete flowfield solutions are the unsteady, incompressible Navier-Stokes equations, written in the tensor notation as below, where the indices $i = 1,2,3$ represents the $x_1(x), x_2(y)$ and $x_3(z)$ directions, respectively; while the velocity components are denoted by $u_1(u)$, $u_2(v)$ and $u_3(w)$ respectively. These equations are non-dimensionalized using appropriate velocity $\left(\overline{V}_j\right)$ and length scale (d) where Re represents the Reynolds number.

$$\frac{\partial u_i}{\partial x_i} = 0$$

$$\frac{\partial u_i}{\partial t} + \frac{\partial u_i u_j}{\partial x_j} = -\frac{\partial p}{\partial x_i} + \frac{1}{\mathrm{Re}} \frac{\partial^2 u_i}{\partial x_j \partial x_j}$$

A finite-difference based Cartesian grid immersed boundary solver capable of simulating flows with 3D complex, stationary and moving boundaries is used[24, 25]. The Navier-Stokes equations are discretized using a cell-centered, collocated (non-staggered) arrangement of primitive variables (u, v, w, p). The equations are integrated in time using a second-order accurate fractional step method. A second-order Adams-Bashforth scheme is employed for the convective terms and the diffusion terms are treated using an implicit Crank-Nicolson scheme that eliminates

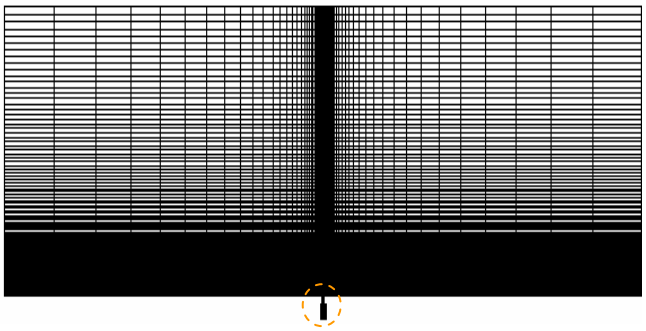

Figure 2a. Domain grid in XY plane (Quiescent jet)

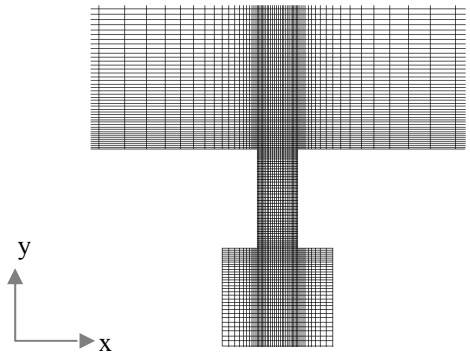

Figure 2b. Grid in jet region

the viscous stability constraint. The pressure Poisson equation is solved using PetSc which is a Krylov-based solver[34]. The convective face velocities are discretized using the weighted-averaging of the second-order central-difference scheme and second order upwind scheme. The code has been validated for a variety of cases against established experimental and computational data[24,25,26].

IV. Results and Discussions

A. Finite aspect-ratio synthetic jet in quiescent flow

In this section results for synthetic jet of AR=8 exhausting into a quiescent external flow will be presented. Note that in a past study[23] we have reported the evolution of AR=1, 2 and 4 jets and the current study is a continuation of

this previous work. The current simulation was performed at a Reynolds number, $\mathrm{Re}_j = 300$ and Stokes number, $S = 6.84$. The Stokes number is representative of typical values used in the experiments[27]. Isosurfaces of the imaginary part of the complex eigenvalue of the velocity gradient tensor[28] during sixth cycle are shown in figure 3 for four different phases. In the earlier phase of expulsion shown in figure 3(a), the rectangular vortex ring emerging from the slot forms a nearly circular vortex ring which is connected to the slot by a rectangular shear layer. Note also that this vortex is clearly separated from the vortices of the previous cycle which have at this point moved far downstream from the jet. At a later stage in the expulsion shown in figure 3(b) the intial circular vortex is still visible although it has convected a significant distance from the slot so much so that it has nearly caught up with the vortices from the previous cycle. In addition to the circular vortex a number of other vortices have formed upstream including a strong elongated vortex which is rotated 90 degrees from the slot. This is indicative of an "axis-switching" phenomenon which will be examined in detail in a subsequent section. At a later stage in the cycle when flow is being ingested into the cavity (figure 3(c)) we observe that the expelled vortices has evolved into a complex vortex cluster which contains in addition to the circular and elongated vortex, a sequence of hairpin-like vortices which are oriented along as well as perpendicular to the slot length. These vortices are formed due to the stretching of vortex filaments by the underlying strain field induced by the jet. At a later stage in the cycle (figure 3(d)) the vortex cluster has convected further downstream and vortex strength is starting to diminish due to the influence of viscosity.

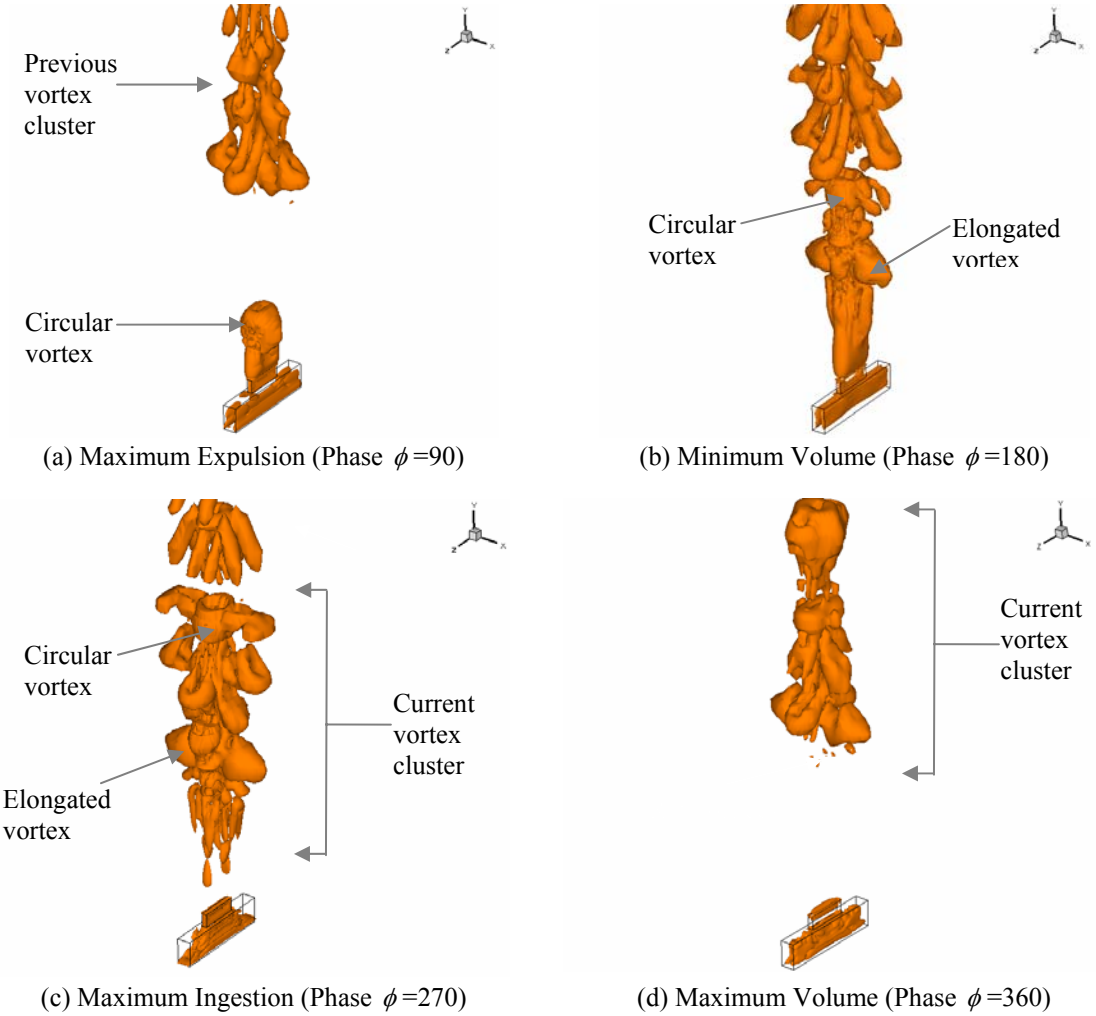

(a) Maximum Expulsion (Phase ϕ=90)

(b) Minimum Volume (Phase ϕ=180)

(c) Maximum Ingestion (Phase ϕ=270)

(d) Maximum Volume (Phase ϕ=360)

Figure 3. Isosurfaces of eigenvalue contours for jet aspect ratio 8

Figure 4 shows a time-sequence of snap-shots of vorticity (ξ) contours in the *XZ*-plane (as viewed from the top) as the jet evolves. This sequence is very illuminating as it shows the various topologies that the jet exhibits at various stages in its evolution. Initially the jet is rectangular but then rapidly transforms to a nearly circular shape. Subsequently the jet seems to switch its axis and become primarily oriented perpendicular to the jet slot. The final topology of the jet seems to be a four-fold symmetric shape which can be seen in figure 4(f).

Isosurface of the mean streamwise velocity of the jet is shown in figure 5 along with the contours at different streamwise stations. The velocity contours appear quite similar to the vorticity contours in figure 4 and show the distinct topologies observed in the jet. Velocity profiles at different streamwise locations along the short and the long axis are shown in figure 6 for $\phi = 90^0$. Note that the profiles are off set successively by adding a constant value to the actual velocities. At the jet exit, the streamwise velocity reaches a peak value and as we proceed downstream the velocity peaks decrease and the jet width increases. Notice that the velocity profiles appear smooth and peaky along the short axis whereas along the long axis it appears more like a plug profile. The distance of the first axis switching can be obtained by plotting the jet width, B_e, in the streamwise direction along the minor and the major-axis[35] and these widths are plotted in figure 7 as a function of the non-dimensional streamwise distance. Note that based on this metric, we determine that the first axis-switching occurs far downstream at $y/\sqrt{A_e} \approx 12$. The subsequent axis-switching of non-isolated vortex rings depends on strong interactions between azimuthal and streamwise vorticity and may vary with the jet aspect ratio and forcing Strouhal number frequency as well. This is beyond the scope of the current study and therefore will not be discussed here.

B. Infinite aspect-ratio synthetic jet in a cross-flow

It has been argued[30] that the effectiveness of synthetic jets can be enhanced by operating them at a forcing frequency in the range of Tollmien-Schlichting (TS) frequencies. One of the objectives here is to determine the effectiveness of synthetic jets operating at forcing frequencies much lower than the TS frequency for a given Re_δ (or Re_{δ^*}). This is because it is not always possible to operate the synthetic jets at or near the TS frequencies, particularly when the TS frequency for a given Re_δ is high enough that operating the actuators at such frequencies may not be possible due to such effects as actuator cavity resonance. Computations have been performed for an infinite aspect-ratio slot with $\mathrm{Re}_d = 200$, $\bar{V}_j/U_\infty = 0.1$ and a range of Stokes numbers. In these simulations we actually assume a

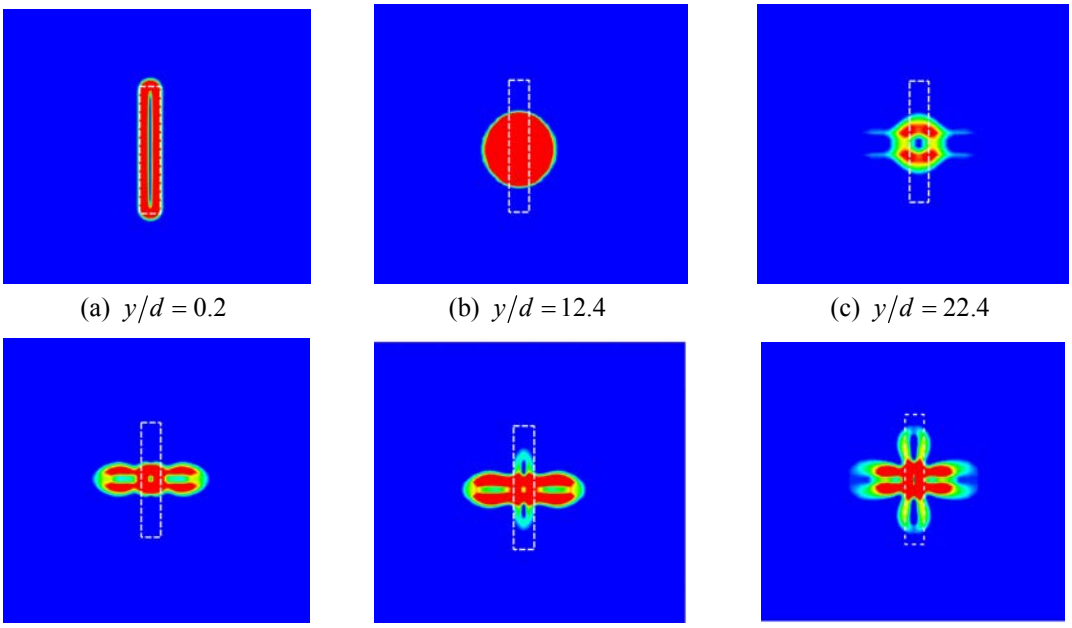

(a) $y/d = 0.2$ (b) $y/d = 12.4$ (c) $y/d = 22.4$

(d) $y/d = 37.4$ (e) $y/d = 39.9$ (f) $y/d = 52.4$

Figure 4. Time sequence of evolution of vorticity (ξ) contours for jet with AR=8 jet.

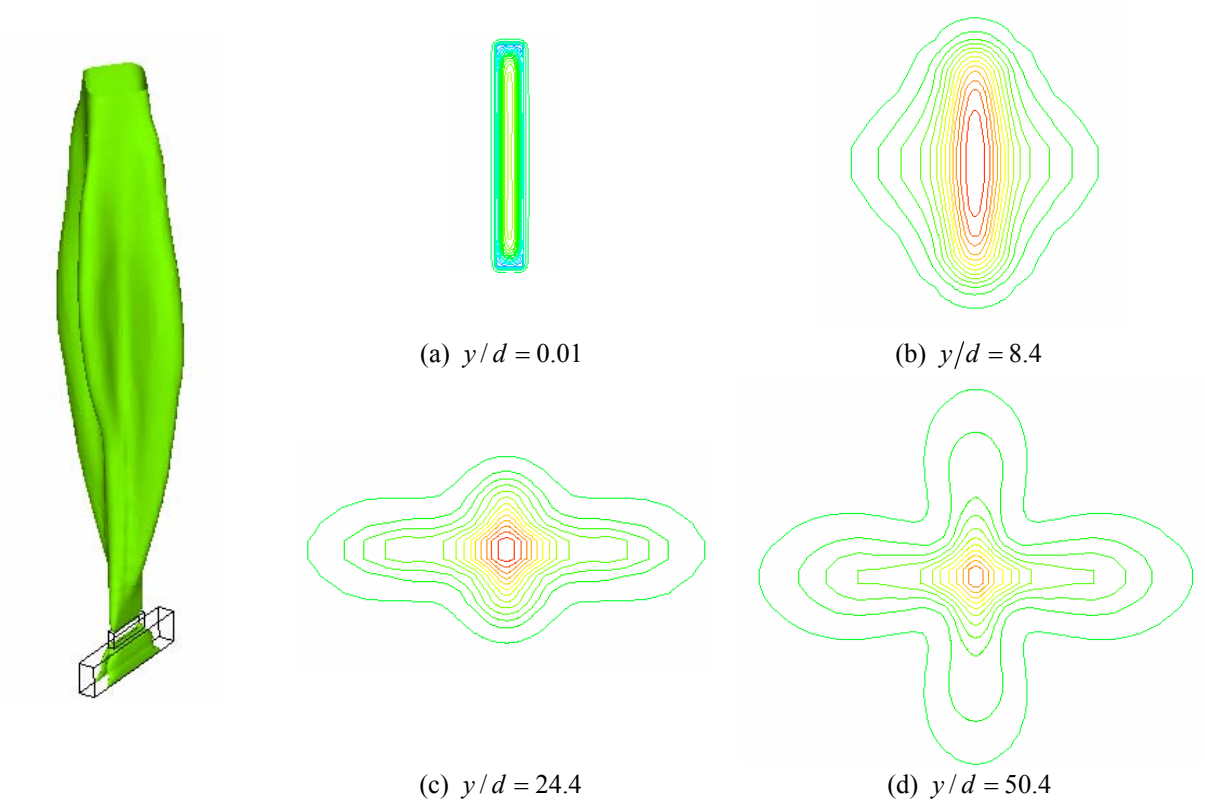

Figure 5. Isosurface of mean streamwise velocity

finite spanwise extent with $L_z = 4$ and apply periodic boundary condition on the spanwise boundary (refer figure.1b). The boundary layer Reynolds number Re_δ is fixed at 4000 and δ/d is 2.0. The value of Reynolds number chosen is slightly above the critical value for a flat plate boundary layer and is therefore expected to be prone to instability.

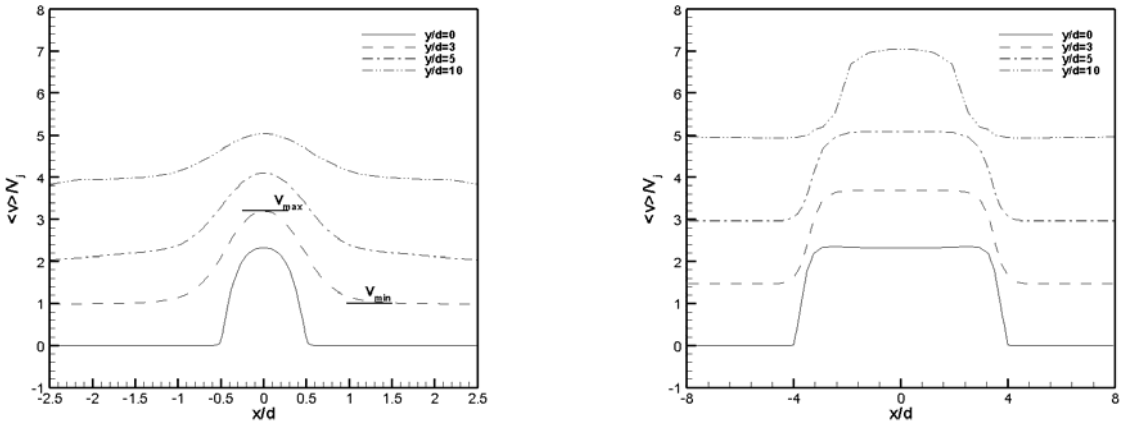

Figure 6. Streamwise phase averaged jet velocity at $\phi = 90^o$ in the (a) x-dir (b) z-dir

From the curves of neutral stability[31] for a flat-plate boundary layer we estimate that the unstable wave number $\left(\alpha\delta^*\right)$ at this Reynolds number ranges from 0.135 to 0.312. Using this wave number range along with the freestream velocity gives a most unstable frequency range, expressed in terms of Stokes number $S = \sqrt{\omega_{TS} d^2/\upsilon}$,

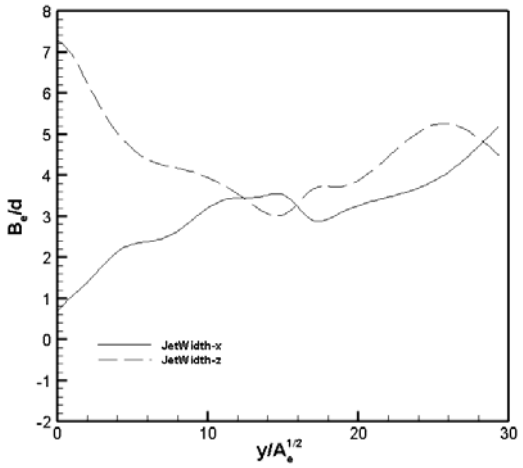

Figure 7. Evolution of jet half-width vs. streamwise direction

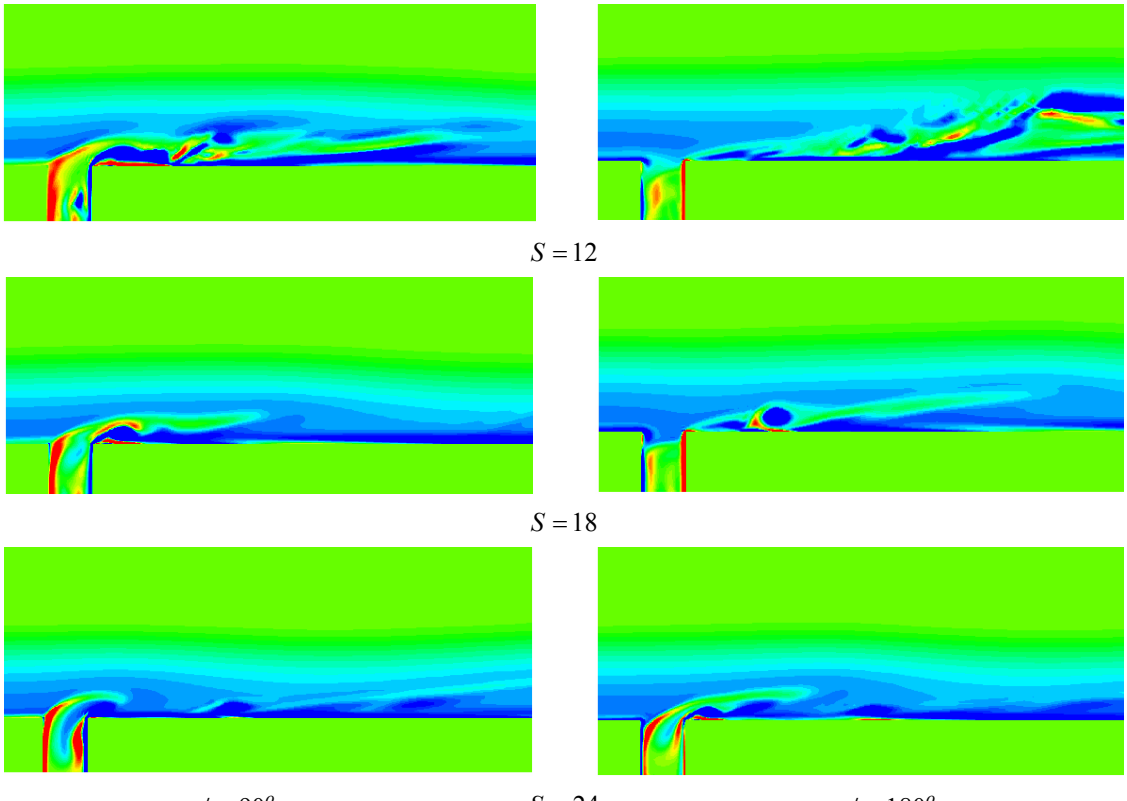

Figure 8 Instantaneous vorticity contours (ξ_z) of a jet interacting with an external boundary layer (Re_d=200)

going from 20 to 31. A non-uniform grid of size indicated in the table 1 is used here with 24×40 grid points in the clustered jet exit region.

Figure 8 shows the vorticity contours (ξ_z) in the xy-plane at the center in the spanwise direction for the maximum expulsion and the minimum volume phases for three different Stokes numbers 12, 18 and 24, considered.

Note that this range of forcing frequencies is mostly lower than the corresponding most unstable frequencies although the highest forcing frequency does cross into the unstable range. The spanwise contour plots indicate the most vigorous response at the lowest Stokes number. The time-mean velocity profiles, taken over last 4 cycles, downstream of the jet exit plane are plotted in figure 9. Superimposed on these profiles is the Blasius boundary layer profile at the inlet which is also the cross-flow velocity. It is noted from these profiles that velocity increases in the boundary layer in the neighborhood of the jet downstream indicating the addition of momentum in the near jet region. This is due to the entrainment of the fluid from the high momentum external flow by the vortices. It is also observed from these figures that the momentum addition reduces with the increase in the Stokes number. This could be attributed to the fact that the vortex structures emanating from the jet are smaller and weaker for $S = 24$ than for $S = 12$ or 18 and therefore less capable of entraining outside flow. As Stokes number increases with fixed Reynolds number, the vorticity flux from the jet reduces[29] and also the ratio Re/S^2 reduces, thereby, tending to the limiting value below which there will be no jet-formation for axisymmetric jets[32]. The response of the boundary layer to the forcing can also be examined by considering the turbulent kinetic energy in the boundary layer as shown in figure10.

It is clear from this plot that the response to the $S = 12$ jet is quite robust where the boundary layer does not seem to respond at all to the $S = 18$ forcing. For the $S = 24$ the boundary layer response in the near vicinity of the jet is quite limited although further downstream the flow does seem to exhibit an increased level of fluctuations. Thus despite the lower frequency being significantly below the most unstable frequency, we observe a robust response primarily due to the fact that the vorticity flux from the jet is highest at this lower frequency.

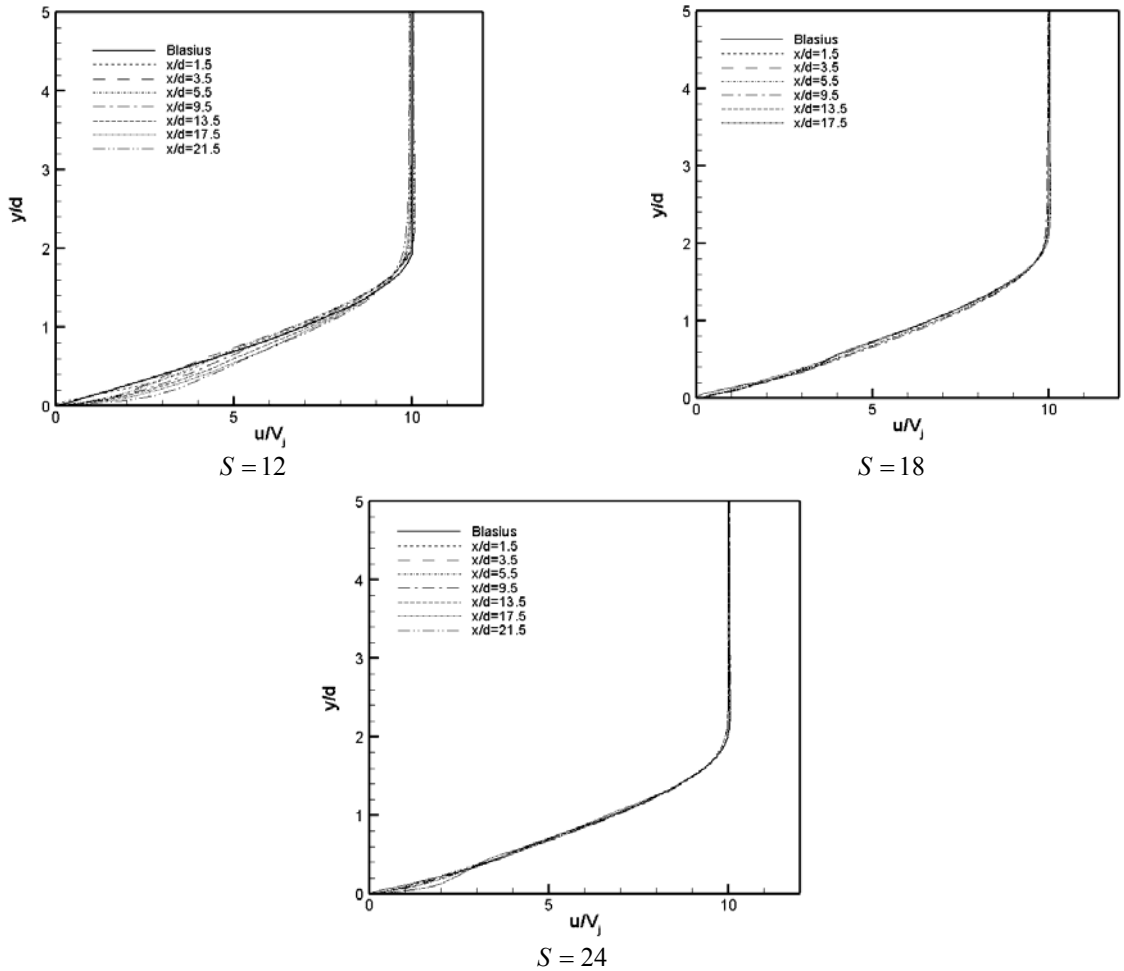

$S = 12$ $S = 18$

$S = 24$

Figure 9. Time-mean velocity profiles in the downstream region of jet exit

This response of the boundary layer to the forcing can be characterized in terms of its displacement and momentum thickness and the shape factor as shown in figure 11. For a laminar boundary layer with zero pressure

gradient $\delta^* \approx \delta/3$ and $\theta = 2\delta/15$. Note that the corresponding displacement thickness values for Blasius $\left(\frac{u}{U_\infty} = \frac{3}{2}\eta - \frac{1}{2}\eta^3\right)$ and turbulent flow velocity $\left(\frac{u}{U_\infty} = \eta^{1/7}\right)$ profiles are also superimposed on these plots. From

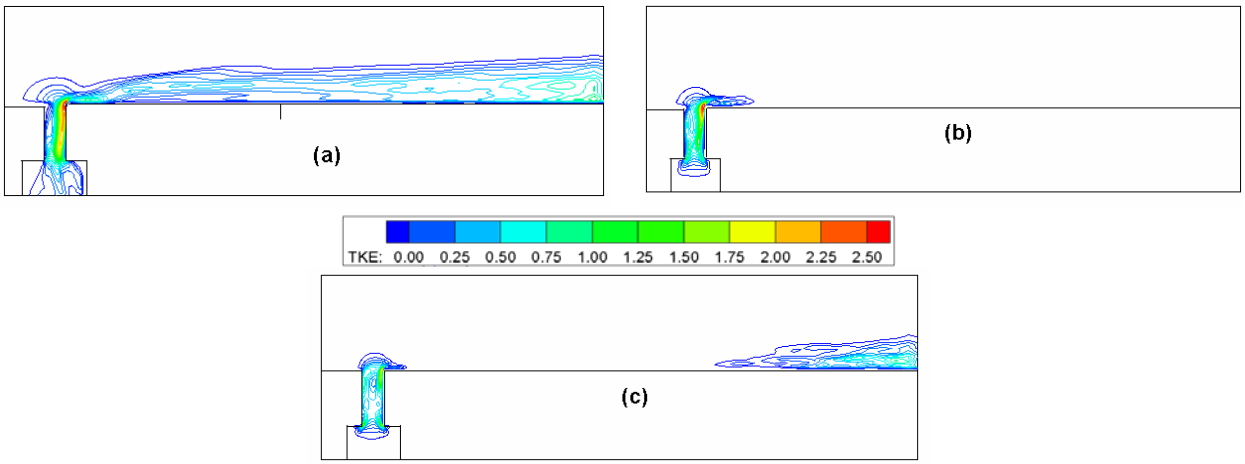

Figure 10. Contours of turbulent kinetic energy (a) $S = 12$, (b) $S = 18$, (c) $S = 24$

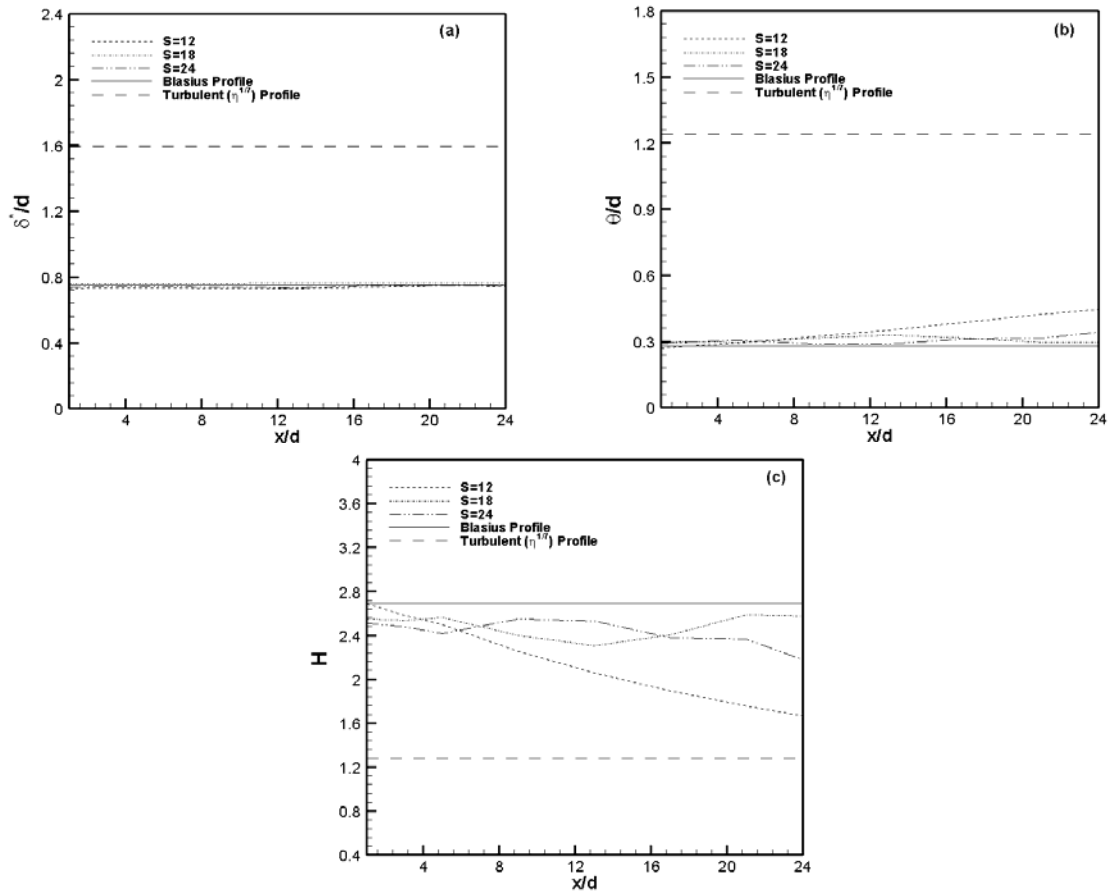

Figure 11. Variation of (a) displacement thickness (b) momentum thickness and (c) shape factor in the jet downstream

figure 11(a) it is clear that displacement thickness shows little variation from the laminar value with the Stokes number. This is not surprising given the zero-net mass flux character of the forcing. However, it is observed that the momentum thickness for $S = 12$ increases linearly along the downstream region in comparison with $S = 18$ and $S = 24$ for which they are in the range of 0.27 to 0.32. The flow behavior in the downstream regions of the jet can be better explained in terms of the shape factor H, whose variation with x is shown in figure 11(c). It should be noted that H is smaller $(H \approx 1.3)$ for a turbulent boundary layer than for a laminar boundary layer[33] $(H = 2.6)$ for a flat plate at zero incidence. Shape factor is associated with the pressure gradient and its value increases to approximately 2.5 and 3.5 at separation for turbulent and laminar boundary layer respectively. Therefore, smaller H is good in terms of avoiding separation because it implies higher transverse momentum exchange in the boundary layer. In other words, higher momentum fluid further away from the wall is brought closer to the wall. This fluid has more streamwise momentum and is therefore capable of coping with adverse pressure gradients. It is therefore an indication of how prone a boundary layer is to separation. Notice that for $S = 12$ the shape factor continuously decreases in the downstream region and seems to be approaching the value corresponding to turbulent boundary layer. However, for $S = 18$ or 24, H lies between 2.4 and 2.6 indicating no significant momentum addition in the downstream regions.

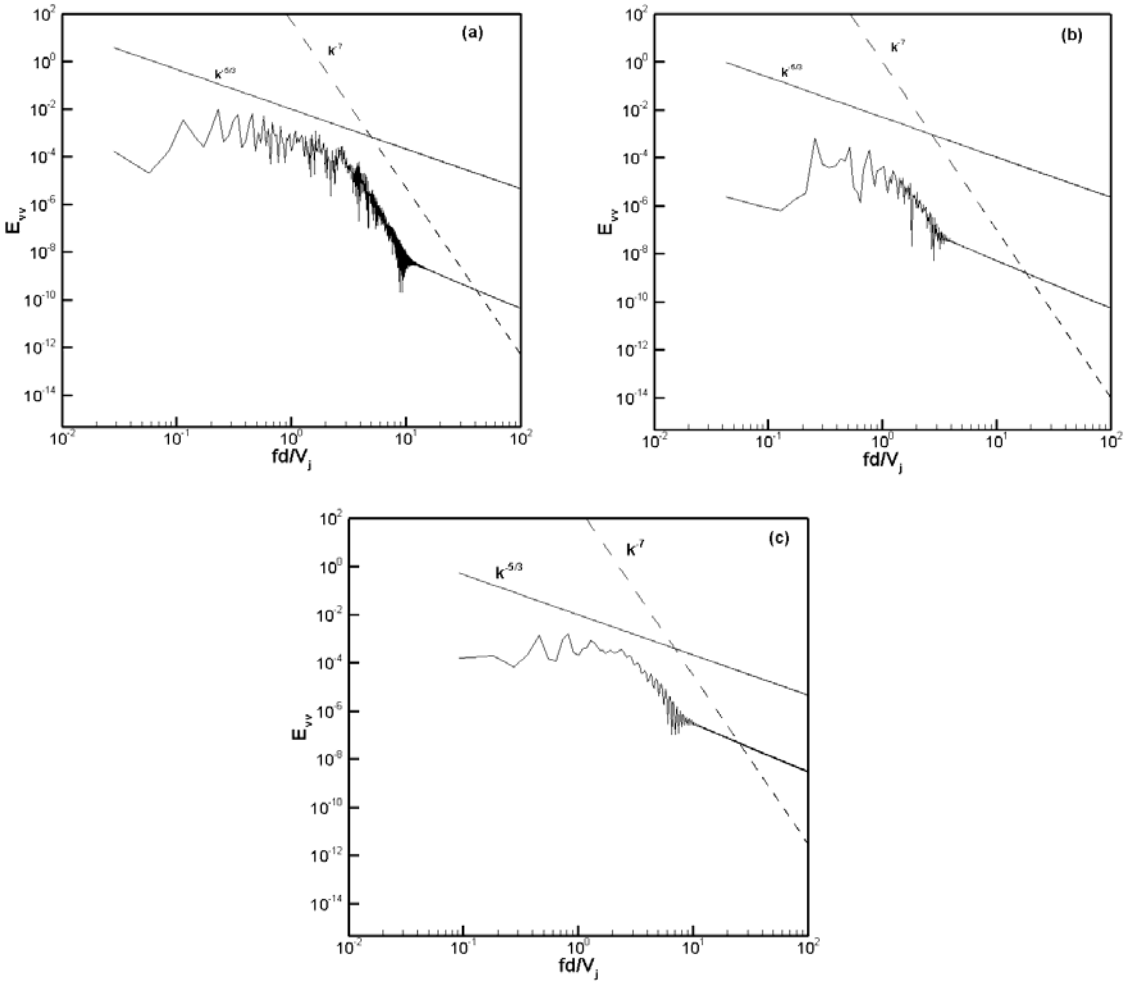

Figure 12. Frequency spectra corresponding to turbulent fluctuation v' along the centerline at $x/d = 9.5$ from jet center (a) $S = 12$ (b) $S = 18$ (c) $S = 24$

Frequency spectra for all the three cases are shown in figure 12 at $x/d = 9.5$ where the coordinate axis is centered at the jet exit in *x-y-z* directions. The probe data location is shown in figure 10(a) as a short vertical line on

the flat surface. The frequency f in these plots is non-dimensionalized by $\bar{V}_j/d$ and the spectrum $E_{vv}(f)$ is obtained by normalizing the spectral density by $2\pi f$. The spectrum for $S=18$ and 24, the frequencies of which are in the range of TS frequency, is included for the sake of completeness in comparison with $S=12$. Also included in these plots are the lines corresponding to $k^{-5/3}$ and k^{-7} variations. The $k^{-5/3}$ variation is associated with the inertial subrange and k^{-7} represents the dissipative range. From the frequency spectra plots it is clear that noticeable inertial subrange as well as a distinct dissipation range is visible for $S=12$ whereas there are no such indications for the cases with $S=18$ and $S=24$ concurring with the analysis presented from the velocity profiles and the boundary layer characteristics. The fact that this happens at a lower than TS frequency is somewhat unexpected but it should be noted that the current perturbations are not small by any measure and therefore the response of the boundary layer is not necessarily governed by small perturbation theory. Secondly the vorticity flux from the jet, which plays an important role in disturbing the boundary layer, is highest for the lower Stokes number and this might also account for the higher response at this Stokes number. The issue regarding the scaling of the vorticity flux with frequency is addressed next.

Recently, it has been shown for a synthetic jet in a cross-flow, the vorticity flux, defined as $\Omega_V = \int_0^{T/2}\int_0^{d} |\xi_z|\, v\, dxdt$ where ξ_z is the z-component of vorticity for two-dimensional flows, scales with other non-dimensional parameters like jet Reynolds number, Stokes number, δ/d and $\bar{V}_j/U_\infty$. An explicit scaling law has been derived and has the form[29]:

$$\frac{\Omega_v}{\bar{V}_j d} = \alpha(\mathrm{Re}) St^{-\beta}\left(\lambda + \frac{U_\infty}{\bar{V}_j}\right)$$

For 2D simulations values of λ and β are found to be 3.9 and 0.9 respectively and $\alpha(\mathrm{Re}_j) = 0.66 \times \ln\left(\frac{\mathrm{Re}_j}{4.04}\right)$.

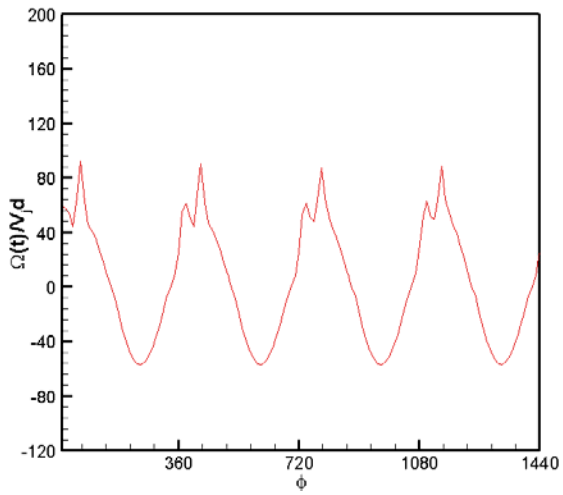

Figure 13(a). $\Omega(t)$ variation with phase

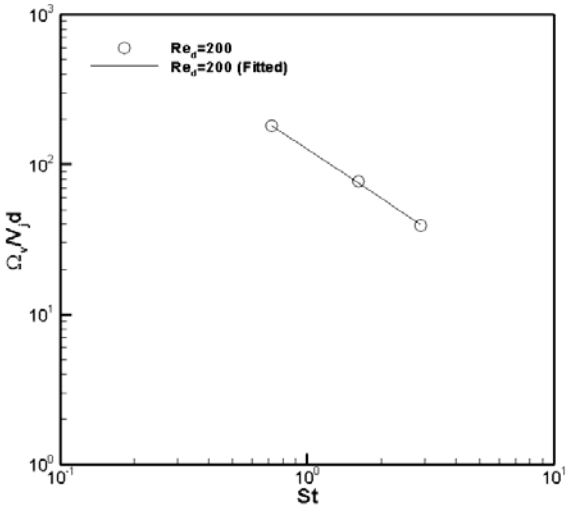

Figure 13(b). Vorticity flux as a function of Strouhal number

Since these were derived based on the two-dimensional simulations[29], the question is whether they hold good for three-dimensional case as well. In particular, it is important to assess the variation of the vorticity flux with the jet frequency (and therefore the Strouhal number). For three-dimensional cases ξ_z is replaced by $\xi = \sqrt{\xi_x^2 + \xi_y^2 + \xi_z^2}$ in the definition of Ω_v. The computed non-dimensional vorticity flux values based on the above simulations is presented in figure 13 as a function of phase for four cycles for $S=24$. The periodic repetitions indicate that the flow has reached a stationary state. Figure 13(b) shows a plot of the vorticity flux during expulsion plotted against Strouhal number on a log-log plot. The plot clearly shows a power law behavior and a best fit line indicates an

exponent (β) of -1.1 which is indicative of an inversely proportional variation as in the 2D case. Since the Strouhal number is also equal to S^2/Re we expect that the vorticity flux for the $S = 24$ case will be about four times smaller than the $S = 12$ case and this might be the reason why the lower frequency perturbation leads to a larger response in the boundary layer.

V. Conclusion

Formation and evolution of synthetic jet of aspect-ratio (AR) 8.0 is analyzed for a jet issuing into quiescent air and it is found that the vortex train emanating from the jet exit undergoes axis-switching and assumes a complex shape. The mean structure of the jet indicates the jet spreading that would be helpful in mixing and entrainment of the ambient fluid. Simulation for an infinite aspect-ratio jet interacting with an external Blasius boundary layer indicate that actuation frequencies much lower than the Tollmein-Schlichting frequencies are effective in triggering instabilities in the boundary layer which might transition the flow. The results also indicate that vorticity flux varies linearly with the inverse of the Strouhal number.

Acknowledgments

This work was supported from Air Force Office of Scientific Research grant FA 9550-05-1-0169

References

[1]Smith, B. L., and Glezer, A., "Jet Vectoring Using Synthetic Jets", *Journal of Fluid Mech.,* Vol. 458, 2002, pp. 1-34.

[2]Lee, C. Y., and Goldstein, D. B., "DNS of microjets for Turbulent Boundary Layer Control", *AIAA* 2001-1013, 2001.

[3]Rathnasingham, R. and Breuer, K. S., "Active Control of Turbulent Boundary Layers", *Journal of Fluid Mech.,* Vol. 495, 2003, pp. 209-233.

[4]Rathnasingham, R. and Breuer, K. S., "System Identification and Control of a Turbulent Boundary Layer", *Phys. Fluids A,* Vol. 9, No. 7, 2003, pp. 1867-1869.

[5]Davis, S. A., Glezer, A., "Mixing Control of Fuel Jets Using Synthetic Jet Technology: Velocity Field Measurement", *AIAA* 99-0447, 1999.

[6]Chen, Y., Liang, S., Anug, K., Glezer, A., and Jagoda, J., "Enhanced Mixing in a Simulated Combustor Using Synthetic Jet Actuators", *AIAA* 99-0449, 1999.

[7]Smith, D., Amitay, M., Kibens, V., Parekh, D., Glezer, A, "Modification of Lifting Body Aerodynamics Using Synthetic Jet Actuators", *AIAA* 98-0209, 1998.

[8]Amitay, M., Kibens, V., Parekh, D., and Glezer, A., "The Dynamics of Flow Reattachment Over a Thick Airfoil Controlled by Synthetic Jet Actuators", *AIAA* 99-1001, 1999.

[9]Smith, B. L., and Glezer, A., "Vectoring and Small-Scale motions Effected in Free Shear Flows Using Synthetic Jet Actuators", *AIAA* 97-0213, 1997.

[10]Mittal, R., and Rampunggoon, P., "On Virtual Aero shaping Effect of Synthetic Jets", *Phys. of Fluids,* Vol. 14, No.4, 2002, pp. 1533-1536.

[11]Mittal, R., Rampunggoon, P., and Udaykumar, H. S., (2001), "Interaction of a Synthetic Jet with a Flat Plate Boundary Layer", *AIAA* 2001-2773, 2001.

[12]Meissner, A., "Uber Piezo-Elektrische Kristalle bei Hoch-Frequenz", *Zh. Tekh. Fiz*, Vol. 7, 1926, pp. 585

[13]Andres, J. M., and Ingrad, U., "Acoustic Streaming at High Reynolds Numbers*", J. Acoust. Soc. Am.*, Vol. 25, No. 5, 1953, pp. 928-932

[14]Ingrad, U., and Labate, A., "Acoustic Circulation Effects and the Nonlinear Impedance of Orifices", *J. Acoust. Soc. Am.,* Vol. 22, No. 2, 1950, pp. 211-218

[15]Lebedeva, I. V., "Experimental Study of Acoustic Streaming in the vicinity of Orifices", *Soviet Phys. Acoust.,* Vol. 26, No. 4, 1980, 1980, pp. 331-333

[16]Sheen, S. H., Lawrence, W. P., and Raptis, A. C., "Cavitation-Controlled Ultrasonic Agitator", *Proc. IEEE Ultraosnics Symposium*, Vol. 1, 1989, pp. 653-656.

[17]Yao, C. S., Chen, F. J., Neuhart, D., and Harris, J., "Synthetic Jets in Quiescent Air", *Proc. NASA LaRC Workshop on CFD Validation of Synthetic Jets and Turbulent Separation Control*, Williamsburg, Virginia, March 29-31, 2004

[18]Kral, L. D., Donovan, J. F., Cain, A. B., and Cray, A. W, "Numerical Simulaiton of Synthetic Jet Actuators", *AIAA* 97-1824, 1997

[19]Rizzetta, D. P., Visbal, M. R., and Stanek, M. J., "Numerical Investigation of Synthetic-Jet Flowfields", *AIAA Journal,* Vol. 37, No. 8, 1999, pp. 919-927

[20]Rampunggoon, P., "Interaction of a Synthetic Jet with a Flat Plate Boundary Layer", Ph. D Dissertation, University of Florida, Gainesville, FL, 2001.

[21]Utturkar, Y., Mittal, R., Rampunggoon, P., and Cattafesta, L., "Sensitivity of Synthetic Jets to the Design of the Jet Cavity", *AIAA* 2002-0124, 2002.

[22]Holman, R., Utturkar, Y., Mittal, R., Smith, B. L., and Cattafesta, L., "Formation Criterion for Synthetic Jets", *AIAA Journal,* Vol. 43, No. 10, 2005

[23]Ravi, B. R., Mittal, R., and Najjar, F. M., "Study of Synthetic Jet Flow fields Using Three-Dimensional Numerical Simulation", *AIAA* 2004-0091, 2004

[24]Bozkurttas, M., Dong, H., Seshadri, V., Mittal, R., Najjar, F., "Towards Numerical Simulation of Flapping Foils on Fixed Cartesian Grids", *AIAA* 2005-0079, 2005

[25]Kotapati, R.B., Mittal, R., "Time-Accurate Three-Dimensional Simulations of Synthetic Jets in Quiescent Air", *AIAA* 2005-0103, 2005

[26]Najjar, F. M., and Mittal, R., "Simulation of Complex Flows and Fluid-Structure Interaction Problems on Fixed Cartesian Grids", FEDSM2003-45577, *Proc. FEDSM' 03, 4th ASME-JSME Joints Fluids Engineering Conference*, Honolulu, Hawaii, pp. 184-196, 2003.

[27]Smith, B. L., and Glezer, A., "The formation and evolution of synthetic jets", *Physics of fluids*, Vol. 10, No. 9, 1998, pp. 2281-2297

[28]Jheong, H., and Hussain, F., "On the Identification of a vortex", *Journal of Fluid Mechanics,* Vol. 285, 1995, pp. 69094

[29]Raju, R., Mittal, R., Gallas, Q. and Cattafesta III, L.N., "Scaling of Vorticity Flux and Entrance Length Effects in Zero-Net Mass-Flux devices", *AIAA* 2005-4751, 2005.

[30]Hong, G., Lee, C., Ha, Q, P., Mack, A. N. F., and Mallinsion, S. G., "Effectiveness of Synthetic Jets Enhanced by instability of Tollmien-Schlichting Waves", *AIAA* 2002-2832, 2002

[31]Schlichting, H., *Boundary Layer Theory*, 4th ed., McGraw-Hill, New York, 1960.

[32]Utturkar, Y., Holman, R., Mittal, R., Carroll, B., Sheplak, M., and Cattafesta, L., "A Jet Formation Criterion for Synthetic Jet Actuators", *AIAA* Paper 2003-0636, 2003

[33]Fox, R. W., and McDonald, A. T., *Introduction to Fluid Mechanics*, 5th Ed., John Wiley & Sons, New York, 1998.

[34]Balay, S., Gropp, W. P., McInnes, L, C., and Smith, B. F., (2000), "PetSc 2.0 Users Manual", Argonne National Laboratory, ANL-95/11-Revision 2.0.29, 2000.

[35]Miller, R. S., Madnia, C. K., and Givi, P., "Numerical Simulation of Non-Circular Jets", *Computers & Fluids*, Vol. 24, No. 1, 1995, pp. 1-25